

## Accurate determination of low-symmetry Bravais unit cells by EBSD

Ming Han<sup>a,\*,#</sup>, Guangming Zhao<sup>b,a,#</sup>, Ye Zhu<sup>b\*</sup>

<sup>a</sup>School of Materials Science and Engineering, East China Jiaotong University, Nanchang

330013, Jiangxi, China

<sup>b</sup>Department of Applied Physics, The Hong Kong Polytechnic University, Hung Hom,

Kowloon, Hong Kong, China

### Abstract

Unit cells lack of symmetry are difficult to determine accurately, compared to high-symmetry unit cells with many constraints. The electron backscatter diffraction (EBSD) technique in scanning electron microscopy (SEM) was considered inadequate for this task because of the highly defective band detections. We develop a new method for the Kikuchi-band detections, which can improve the accuracy of the EBSD technique in determining the lattice constants of totally unknown Bravais unit cells with low symmetry. The results show that, under ideal conditions (i.e., low-noise EBSD patterns and known projection center), the relative error of the unit-cell constants ( $a$ ,  $b$ ,  $c$ ) is less than 0.3%, and that of the axial ratios ( $a/b$ ,  $b/c$ ,  $c/a$ ) is less than 0.5%. The absolute errors of the inter-axial angles ( $\alpha$ ,  $\beta$ ,  $\gamma$ ) and crystal orientations are about  $0.1^\circ$ . Our method is perhaps not as accurate as the classical techniques such as X-ray diffraction, but is demonstrated as a practical tool for crystallographic characterization

---

\* Correspondence e-mail: [mhancn@yahoo.com](mailto:mhancn@yahoo.com) (Ming Han) and [yezhu@polyu.edu.hk](mailto:yezhu@polyu.edu.hk) (Ye Zhu)

# These authors contributed equally to this work.

especially on low-fraction phases, and could be easily incorporated into an SEM to make the most of the SEM in the area of microanalysis.

**Keywords:** triclinic; low symmetry; unit cell; lattice constants; EBSD; Kikuchi pattern

## 1. Introduction

Crystals are built up by an orientational stacking of very small regular ‘brick-like’ unit cells. Edges of the unit cells are considered to be parallel to the three axial vectors ( $\vec{a}$ ,  $\vec{b}$ ,  $\vec{c}$ ) of the seven crystal systems which are subdivided into 14 Bravais-lattice types according to different symmetries. In general, lattice constants are sensitive to a variety of external and internal conditions, such as temperature, stress, chemical composition, etc. Accurate determination of the Bravais unit cells (including their symmetries and lattice constants) is prerequisite to phase identification, calculating the atomic distance and bond energy, and analyzing the relations between lattice constants and various physical/chemical properties.

However, accurate determination of the Bravais unit cells is not trivial even for the cubic system with many symmetry constraints, and it becomes more difficult for the low-symmetry crystal systems, especially the triclinic one [1-3]. For the crystalline materials with low symmetries, their crystal structures are generally complex and often accompanied by relatively poor crystalline perfection with residual stress and fine grain size. These characteristics make their diffraction patterns complicated and any tiny error or mishandling in the data processing will severely impact the accuracy and reliability of the final determination results [4, 5]. Take the X-ray diffraction (XRD) technique as an example, the best accuracy of measuring the lattice constants for cubic

system is about 0.0005%, which is close to the accuracy of measuring the X-ray wavelength and thus is possibly so far the limit of measuring lattice constants [6, 7]. In ordinary cases, the measurement accuracy for cubic system is about 0.002% [8, 9]. For triclinic system, however, the best accuracy, under the condition of no systematic errors (e.g., instrumental misalignment, incident beam divergence, off-center specimen, specimen absorption, etc.), is 0.01% [10], one order of magnitude lower than that for cubic system. In practical measurement, it is, of course, not free from sources of the systematic errors. As a result, the measurement accuracy for triclinic system deteriorates even further to about 0.3% [10], two orders of magnitude lower than the ordinary cases for cubic system.

Given the above accuracies of the XRD technique, it is still challenging to characterize the phases with a low fraction because of their insufficient X-ray diffraction signals. In this case, the popular alternative technique is the transmission electron microscopy (TEM). But it requires time-consuming sample thinning and sometimes may not be readily available.

Nowadays, electron backscatter diffraction (EBSD) technique in scanning electron microscope (SEM) is comparatively widespread for microanalysis. It is a locally resolving technique that enables a combination of the microstructural and orientational characterizations, such as morphology and texture based on orientational analysis of known crystals. It nonetheless has an unfavorable reputation of being too inaccurate to measure the lattice constants reliably. For lattice-constant determination, EBSD's best accuracy is considered to be 5%, and the error of the data extracted from EBSD patterns

may be up to 20%, because of the normally vague diffraction patterns and the highly defective band detections [3, 11].

In our previous works, a new three-dimensional reconstruction procedure was reported, which involved as many as possible Kikuchi bands that were visible in an EBSD pattern and built a system of equations (tens of thousands of) for a least-squares solution in order to over-determine the unknown unit cells by using a single EBSD pattern [12-16]. The corresponding determination error was confined mainly by building the overdetermined system of equations. Although the obtained accuracy (about 1% for lattice constants [17]) is reasonably high, the adopted band-detection method remains inherently unsatisfying and the accuracy was derived only from cubic and tetragonal unit cells. In this work, we propose an improved method for the Kikuchi-band detections, which utilizes the crystallographic information extracted from an EBSD pattern to further confine the determination error. Then we apply this new method to determine low-symmetry unit cells. The obtained accuracies for materials with triclinic unit cells are better than 0.3% for both the unit-cell constants ( $a$ ,  $b$ ,  $c$ ) and the axial ratios ( $a/b$ ,  $b/c$ ,  $c/a$ ), better than  $0.3^\circ$  for the inter-axial angles ( $\alpha$ ,  $\beta$ ,  $\gamma$ ), and  $0.1^\circ$  for crystal orientations. This is significantly better than the previous accuracy we achieved on high-symmetry cubic or tetragonal materials, demonstrating the great potential of our method for structure determination on SEM.

## **2. Geometric crystallography of EBSD**

EBSD signals emitted from an effective point source inside a crystal sample are gnomonically projected onto a flat screen of the EBSD detector, recording a two-

dimensional Kikuchi diffraction pattern. In this three-dimensional configuration of gnomonic projection, the ratio between the specimen-to-screen distance and the height of the Kikuchi pattern is defined as the detector distance, which affects the pattern's angular coverage  $\varphi$  (Fig. 1a). Typically, a Kikuchi pattern covers an angle  $\varphi$  in the range of 70–100°. A point in the two-dimensional pattern with the shortest distance to the emitting source (i.e., projection center) is usually called the pattern center.

From the crystallographic point of view, a single Kikuchi diffraction pattern provides abundant information about the crystalline phase (including its real and reciprocal unit cells). To be specific, in a Kikuchi pattern tens of bands represent the electron diffraction signals of lattice planes  $(hkl)_i$ . The widths of bands decide the absolute values of the unit-cell constants  $(a, b, c)$  according to Bragg's equation  $2d_{(hkl)} \sin \theta_i = n\lambda$ , where  $\theta_i$  is approximately proportional to the width of a Kikuchi band (Fig. 1b). These Kikuchi bands intersect each other, forming hundreds of Kikuchi poles, namely, zone axes  $[uvw]_m : (hkl)_i \times (hkl)_j = [uvw]_m$ , with  $hu + kv + lw = 0$ . Here, the indices of  $h, k, l$ , and  $u, v, w$ , are all integers, which means that all bands and poles showing visible Bragg diffraction contrast within the angular coverage of a Kikuchi pattern have integer Miller indices. The positions of the diffracting-plane traces and zone axes depend on inter-axial angles  $(\alpha, \beta, \gamma)$ , axial ratios  $(a/b, b/c, c/a)$ , and crystal orientations (e.g., the three Euler angles,  $Z, X, Z$ ). The widths of the Kikuchi bands are associated with the magnitude of lattice constants. The success (including high accuracy and high reliability) of determining the Bravais unit cells based on the EBSD technique is therefore strongly dependent on the accuracy and precision of the adopted

band-detection method. In particular, correctly locating the traces and describing the band widths of diffracting lattice planes are of critical importance.

Unfortunately, it is difficult to accurately determine the traces and widths in a Kikuchi pattern. Owing to the gnomonic projection (Fig. 1), the two edges of each band have a hyperbolic shape, and its width is approximately proportional to twice the Bragg angle ( $2\theta_i$ ) of a diffracting lattice plane  $(hkl)_i$ . The trace of a diffracting lattice plane  $(hkl)_i$ , which is an invisible line of intersection between the  $(hkl)_i$  plane and the Kikuchi pattern, is not coincident with the center line of corresponding hyperbola-shaped Kikuchi band, as illustrated in Fig. 1b. The maximum deviation between a center line and corresponding trace appears to be only few image pixels (about  $0.1^\circ$  within the angular coverage  $\phi$  shown in Fig. 1a) and hence difficult to notice in a Kikuchi pattern. Such inaccuracy in trace positions may not affect the directions of the traces and the angles between them, but will cause considerable errors in the locations of zone axes as well as the following unit-cell determination.

With respect to the widths of Kikuchi bands, it is also difficult to perform an accurate measurement in a Kikuchi pattern because the intensity profiles of the diffraction bands are complex [18]. Thus the lattice spacing  $d_{(hkl)}$  ( $d_{(hkl)}^{-1} \propto \theta_i$ ) obtained from measurement of the band widths tends to be rather imprecise (with error up to 20%). In consequence, using the erroneously measured  $d_{(hkl)}$ , a poorly defined reciprocal primitive cell will be reconstructed, which eventually leads to an inaccurate and unreliable determination of the real unit cell.

In spite of the aforesaid unfavorable features of Kikuchi patterns, accurate determination of the traces and band widths is still achievable. For example, a large amount of zone axes in a single EBSD pattern can be accurately determined (which is why the EBSD technique is widely accepted for accurate crystal orientation analyses). Moreover, if gnomonic distortion of the EBSD pattern was corrected and also the pattern center, detector distance and crystal orientation were accurately known, all trace positions can be correctly calculated. The deviation between the trace and the center line of a hyperbola-shaped band becomes obvious for high-order Kikuchi bands.

Nevertheless, in the case of experimental pattern analysis, the pattern center and detector distance are difficult to determine with high accuracy [5, 19], and not every Kikuchi band shows a high-order feature. In view of these practical reasons (e.g., inaccurate or even unknown projection center), our routine of determining the band edges (or measuring band widths) is mainly composed of two stages.

At the initial stage, we perform measurement with an estimated pattern center and detector distance (their detailed estimation process will be introduced in the next section). Hence, an approximation is made, i.e., the trace and center line are regarded as being coincident (only for initial Kikuchi band detection). Subsequently, we can use a pair of parallel lines and their midline to approximate the hyperbolic band edges and the corresponding trace, respectively. Here the band width  $w_i$  (marked by two arrows in Fig. 1b) is defined as the closest distance between the two hyperbolic edges, and equal to the spacing between the two approximate straight lines.

Given real Kikuchi bands (especially those blurred ones shown in Fig. 2a), their band edges cannot be definitely determined only by their intensity profiles. Hence, we first roughly determine the edges of a Kikuchi band by eye, obtaining a reciprocal lattice vector  $\vec{H}$  whose direction is perpendicular to this band's trace line and whose length is proportional to this band's width (after geometric correction). Often the edge located by eye is close to a point where the grayscale gradient of the band profile attains an extreme value. Then we perform this rough measurement on all bands intersecting at the same zone axis  $[uvw]$  (e.g., the one marked by a blue square in Fig. 2a), obtaining a series of reciprocal lattice vectors  $\vec{H}_i$  on the same reciprocal plane  $[uvw]^*$ . Fig. 2b shows such a reciprocal plane  $[uvw]^*$  with nine reciprocal lattice vectors  $\vec{H}_i$  (perpendicular to corresponding green trace lines in Fig. 2a) after geometric correction. According to the distribution of  $\vec{H}_i$ , we use a two-dimensional grid (the green dashed lines in Fig. 2b) to fit every  $\vec{H}_i$  on  $[uvw]^*$ . In an ideal case, every reciprocal lattice vector will have a length that ends at a node on the fitting grid. Owing to measurement errors, however, the endpoints of  $\vec{H}_i$  will somewhat deviate from the grid nodes. Therefore, we can further correct those  $\vec{H}_i$  (marked by red) with obvious deviations, and repeat above measurements and analyses on all zone axes  $[uvw]_j$  and reciprocal planes  $[uvw]_j^*$  in the EBSD pattern, in order to minimize the total deviation between the endpoints of reciprocal vectors and the nodes on fitting grids. It is this deviation that can be used to effectively determine the lengths of reciprocal lattice vectors and thus their corresponding band edges, especially for those blurred ones (e.g., those marked by red arrows in Fig. 2a) [12, 20].



At the above-mentioned initial stage, we have validated in practice by thousands of tests that a band-width measurement error less than 20% is sufficient to enable a correct determination of the Bravais-lattice types. This is actually one of the advantages (e.g., acceptable band width error of up to 20% and insensitive to pattern center and detector distance) of our previously reported algorithm by which the three-dimensional reconstruction completely depends on the geometric relationship among the reciprocal lattice vectors, rather than on their absolute lengths [12].

At the second stage, which is after a reasonable Bravais-lattice type is achieved, and the pattern center and detector distance are optimized based on the Bravais-lattice type and the indices of all Kikuchi bands and zone axes with respect to the Bravais lattice. It should be noted that Bravais-lattice type, band indices and zone-axis indices are all free from any errors. At this second stage, the straight-line approximation used at the initial stage will be replaced by deduced hyperbolae to describe all Kikuchi bands based on the determined Bravais-lattice type, thus the traces and edges can be located more accurately. Detailed description of this second stage (including the optimization process for pattern center and detector distance) is given in the next section.

Furthermore, although the traces of diffracting lattice planes are invisible, their corresponding Kikuchi bands are visible and the traces must pass through zone axes. Each visible zone axis  $[uvw]$  in a Kikuchi pattern has at least two plane traces passing through it, and any connecting line between two zone axes must also be the trace of a diffracting lattice plane:  $[uvw]_m \times [uvw]_n = (hkl)_i$ . Most importantly, the traces of all diffracting lattice planes and their intersections (zone axes) are highly correlated. The

fundamental law of ‘assembly of zones’ discovered by C. S. Weiss [21, 22] points out that any lattice plane can be derived by predefining only four planes (any three of which are non-tautozonal). Similar to diffracting-plane traces, the widths of visible Kikuchi bands are all highly correlated too: From the knowledge of the lattice-constant ratios, only a single band width enables the description of all lattice constants absolutely. Combined with the relatively accurate angular measurement between the traces (with a typical error  $0.5^\circ$  depending on the image quality of recorded EBSD patterns [3]), the close correlations between the numerous bands and zone axes can be applied to improving the accuracy and reliability of the unit-cell constant extraction, as will be demonstrated below in our method.

### 3. Principles and methodology

Given a certain Kikuchi diffraction pattern, its experimental conditions such as accelerating voltage, detector distance and pattern center are often known. The first step required for determining the unit cell corresponding to this specific Kikuchi pattern is to measure the Kikuchi bands, including their traces (close to their center lines, Fig. 1b), angles between them, and band widths. All the visible bands, regardless of their diffraction intensity, should be considered. This process is the so-called band detection, which can be performed either automatically through certain band detection algorithms (e.g., Hough transform [23]) or manually through the naked eyes. However, there is a problem in both cases. As the band detection goes on, more and more bands will be detected. Their traces should exactly intersect at zone axes, each of which should be one point theoretically. However, for those detected bands, if intersected inside the

pattern's angular coverage, their intersections are usually not one point but distribute around the Kikuchi poles (zone axes), namely, the pole-dispersion problem (Fig. 3a). The origin of this problem is that each band is individually detected, which inevitably causes additional errors every time the position of new uncorrelated band is defined.

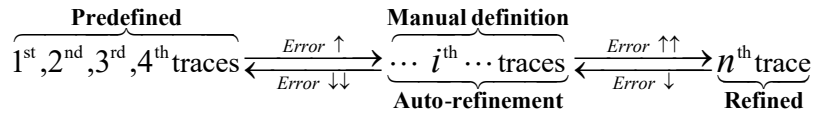
As described in Section 2, following the work by C. S. Weiss, four non-tautozonal planes can uniquely decide all other planes in a crystal lattice. We use this fundamental property to solve the pole-dispersion problem caused by the individual band detection process (Fig. 3a). Specifically, we can identify six zone axes as the intersection points of four traces. Further connecting these six zone axes allows us to locate more traces and subsequently more zone axes. As every intersection point is determined by two trace lines only, the possibility of dispersed intersection points (zone axes) of multiple tautozonal-plane traces can be completely eliminated. In Fig. 3b, the red lines are predefined traces of four non-tautozonal planes, and all the traces belonging to any one zone axis exactly intersect at one point.

Although our approach above can solve the pole-dispersion problem, it heavily relies on an accurate definition of the initial four non-tautozonal plane traces. Any errors in the positions of the initial four traces will be amplified and accumulated during the following trace detection process, which can make an accurate unit-cell determination impossible. Fig. 3b illustrates the ever-increasing error in trace definition of those deduced from the first four hand measured traces. These deduced traces display a perceivable deviation and hence the corresponding band edges. For instance, a green line shifts rightwards compared to the correct blue line, and the pink lines marked by

two arrowheads deviate slightly from the contrast of the band edges, which makes this unit-cell determination unreliable.

Fortunately, the above-mentioned considerable drawback of predefining four traces, i.e., ever-increasing error, could be overturned and become a favorable advantage, i.e., ever-decreasing error. Once again, we exploit the close crystallographic correlation between the bands and zone axes. After the first four trace predefinition, the initial error will be continuously amplified till the last visible band is defined. This last-defined trace (usually far from the initial four traces) has an obvious deviation from its correct position (compared with the visible band edges). Next, we manually decrease this error by refining the definition of the last trace. Then the previous errors of all other traces (including the first four ones) can be collectively decreased since all traces are highly correlated. One benefit of this method is that the positions of all Kikuchi bands' traces can be adjusted collectively and correctly by refining only one or few traces' positions. For example, by refining four intersection points located respectively in the four corners of Fig. 3c, the deviations of all traces and band edges are mitigated obviously as demonstrated by the pink hyperbola segments.

The following procedure briefs our method for limiting the trace-detection errors:



From left to right, it is an error-increasing process, whereas from right to left it is an error-decreasing process. It is important to note that the above procedure may not necessarily be applied to the last defined trace, i.e., a readjustment of any single trace or its intersection points can be used to refine all other traces.

Given a certain EBSD pattern (simulated or experimental), our proposed methodology for band detection is divided into several steps:

- i. Predefine the positions of four non-tautozonal traces, forming six intersection points (i.e., the so-called Kikuchi poles or zone axes). A proper choice of these first four traces (and their initial six intersection points) must guarantee that all visible Kikuchi bands in that EBSD pattern can be defined by way of continuing point-to-point connections.
- ii. Connect the six intersection points to locate more traces and zone axes. This step defines the traces of all visible bands based on the four predefined traces, which is the first demonstration of the ‘law of assembly of zones’ in practice [21, 24].
- iii. Refine the locations of one or more intersection points. The intersections in the four corners of a pattern are recommended to refine first, because they often incline towards obvious deviation.
- iv. Readjust the positions of the four predefined traces based on the redefined zone axes in Step iii, and therefore all bands’ traces can be refined collectively. This step is can be realized (by programming) as an automatic process. If any trace is still apparently deviated from its perceptibly proper position, repeat Steps iii and iv for several zone axes until all traces, especially their intersections, are located correctly.
- v. Measure the widths of all visible bands by using two parallel lines to approximate the band edges. The band width is defined as the closest distance

between the two hyperbolic edges of a band (Fig. 1b). The reciprocal lattice vectors are determined by band widths (after geometric correction) and are further fitted to a two-dimensional grid on a reciprocal plane (Fig. 2). During this step, the band widths are neither accurate nor precise, because of the straight-line approximation. However, one remarkable advantage of this step lies in its insensitiveness to the experimental errors from band width measurement and projection center location. Band widths with a maximum error of 20% are still acceptable, and also a precise location of the projection center is not required, because the three-dimensional reconstruction performed in the next step depends completely on geometric relationship among the reciprocal lattice vectors, rather than on their vector lengths.

- vi. Determine the Bravais unit cell based on the already defined bands. This step essentially consists of four successive sub-steps: (a) reconstruction of a primitive unit cell using all visible Kikuchi bands and zone axes defined as well as a pattern center and detector distance estimated<sup>†</sup>; (b) reduction treatment of the reconstructed primitive cell to find one of the 44 Niggli reduced cells [25]; (c) deducing one of the 14 Bravais unit cells from the obtained reduced cell and indexing all detected Kikuchi bands and zone axes

---

<sup>†</sup> Pattern center (PC) and detector distance (DD) are notoriously difficult to determine with high accuracy [5, 19], but nonetheless both can be preliminarily estimated first and then optimized. Their estimation process is given here, while their optimization will be introduced later. The location of PC can be estimated by all visible Kikuchi bands. Suppose a hyperbolic equation with the form  $x^2/a^2 - y^2/b^2 = 1$  for all Kikuchi bands' edges, where  $(a, 0)$ ,  $(-a, 0)$  are two vertices of the hyperbola on the principal axis  $x$ . The principal axes of all bands' hyperbolic edges always converge at PC. A line from PC to the center  $(0, 0)$  of any hyperbola (band edges) is perpendicular to the trace line. By using this feature in an EBSD pattern, its PC location can be estimated. Once PC is found, DD can be estimated by an iteration in the range of its possible values so long as a three-dimensional reconstruction (all Kikuchi bands can be indexed according to a set of basis vectors) and a possible solution of Bravais lattice can be obtained. The difference between real and calculated band widths must be less than 20% for all Kikuchi bands. At last, DD can be estimated with an error less than 10%.

with respect to the deduced Bravais unit cell; (d) optimization of the previously estimated pattern center and detector distance according to the determined Bravais-lattice type and the indices of all visible Kikuchi bands and zone axes<sup>‡</sup>. Throughout this step, errors are greatly confined and decreased by employing all defined bands and zone axes to build a huge system of overdetermined equations for least-squares analyses. The detailed algorithms corresponding to this step were reported in our previous works [12, 15]. It must be said that although Bravais lattice constants and crystal orientation can be obtained at this step, they are still inaccurate because the zone axes and Kikuchi bands are needed to be carefully matched with hyperbolae. Errors will be further decreased in the following steps.

- vii. Calculate the hyperbolas of all band edges (including their positions, shapes, etc.) based on the determination result obtained in Step vi, and draw an overlay over the EBSD pattern to detect deviations.
- viii. Repeat Steps iii and iv using the calculated hyperbolic edges, if discernable deviation are detected. Once the locations of all zone axes are as much refined as one can, the axial ratios, the inter-axial angles and the crystal orientation, are fixed. Since the locations of zone axes can be ascertained to a relatively

---

<sup>‡</sup> Optimization of both PC and DD is described as follows. The crystallographic reason why this optimization is possible lies in the fact that the deduced Bravais-lattice type is true (if false, it will be explained later) and consequently the indices of all Kikuchi bands and zone axes are completely free of any error. For this reason, we keep the Bravais-lattice type and all those indices unchanged, then perform iterations in the range of possible PC and DD values, with an aim to find the minimum discrepancy between the defined and calculated locations of zone axes. During this process, the zone-axis discrepancy and band-width error will keep decreasing. Once both stop decreasing, the minimum zone-axis discrepancy found must be less than a tolerance factor (discussed later). If so, an optimized PC and DD is obtained. If not, the previously deduced Bravais-lattice type should be wrong and will be excluded from the next unit-cell determination, then a whole determination process from reconstructing a primitive unit cell, (i.e., the sub-step a) needs to be performed again.

high accuracy, the final determination accuracy of aforementioned parameters may reach about 0.5% (depending on pattern quality). After this step, all the constants of a Bravais unit cell can be determined, except the absolute values of the lattice constants ( $a$ ,  $b$ ,  $c$ ) which are decided by the band widths and will be further refined.

- ix. Refine any one band's width (i.e., its Bragg angle) by matching its calculated hyperbola with its visible hyperbolic edges. The band edge will be located by eye at positions where the grayscale gradients of the band profile are believed to have extreme values. In addition, since positioning and measuring of the Kikuchi band traces and widths are pixel-dependent, a higher screen resolution enables this task to be better accomplished in the subpixel scale of the EBSD pattern. Besides, the trace of this diffracting lattice plane can be further adjusted, if necessary (go to Step viii). It is highly recommended that the band chosen to be further refined should have as wide band width and as sharp contrast as possible.
- x. The last step: a final refinement of all bands' widths according to the further refined four non-tautozonal traces as well as one band width can result in the best match between the calculated bands (e.g., their positions, widths, slopes, etc.) and the simulated/experimental bands. The band chosen to be further refined as an auxiliary constraint may have a number of qualified candidates (with wide widths and sharp edges) in a given EBSD pattern. Every candidate band should be entitled to an independent refinement, i.e., repeat Steps ix and



x for different bands, in order to obtain a statistical and convincing determination result.

Overall, for obtaining accurate lattice constants of crystalline materials, measurement of the band widths (diffraction angles) must be accurate first. This requires in turn the same degree of accuracy in the definition of the diffracting plane traces, and then in the locations of zone axes. In other words, locating the zone axes accurately is prerequisite to a reliable Bravais unit-cell determination. Moreover, in experimental patterns which usually have blurred Kikuchi bands, the advantage of our proposed method will become more obvious, since only one relatively clear band is needed, rather than a completely high-quality EBSD pattern, the obtainment of which is quite challenging.

Hereinafter in order to evaluate the above proposed method, we first identify simulated EBSD patterns since they are derived from known unit cells with definite lattice constants and their corresponding crystal orientations and other diffraction conditions are also known, which enables us to precisely evaluate the errors originated mainly from our method. Then, as an important complement to the evaluation, experimentally collected EBSD patterns are also analyzed using the proposed method.

#### **4. Results and discussion**

In this section, we arbitrarily choose four triclinic crystalline materials, then determine their Bravais unit cells by using the method proposed above. The algorithm of this method is programmed using C++ computer language, and embedded into a software *EBSDL* [12, 15]. The crystallographic information files (CIFs) of the chosen

crystals are from literatures [26-29] and all simulated EBSD patterns are acquired with the software DynamicS [30]. Unless stated otherwise in the following, a same set of experimental conditions, namely, accelerating voltage (15 kV), detector distance (0.5), pattern center (0.5, 0.25), pattern resolution (1024×1024 pixels), minimum allowable d-spacing (0.5 Å), minimum intensity ratio (21.0), absorption length (64 Å), excitation depth (50 Å), Debye-Waller factor (0.8 for crystal, 0.3 for source), quality factor (1), thickness (5000 Å), is input into DynamicS for simulation of the four chosen crystals. Another input for the simulation is three Euler angles Z-X-Z (in the Bunge convention [31, 32]) which represent the crystal orientation and are set differently for the four crystals. The simulated patterns are then independently analyzed as completely unknown phases. The determination results (i.e., output of *EBSDL*) include all six constants ( $a$ ,  $b$ ,  $c$ ,  $\alpha$ ,  $\beta$ ,  $\gamma$ ) and three Euler angles ( $Z$ ,  $X$ ,  $Z$ ) of the (unknown) Bravais unit cells. Comparing these independent determination results with the definite reference information in corresponding materials' CIFs, the accuracy of our proposed method could be evaluated. In addition, experimental patterns are also analyzed, and the results further serve as an auxiliary evidence for testing the reliability of our method, though the exact unit-cell constants of the experimental samples may vary slightly according to the material composition, internal stress, etc.

When applying the proposed method to practical pattern determination, there are several sources of errors that need to be paid close attention to, as will be further illustrated below.

The first issue is the tolerance of zone-axis discrepancy. Here a tolerance factor is defined to be the permissible maximum discrepancy between the zone axes manually defined (based on the EBSD pattern) and those calculated (based on the diffracting-plane traces calculated according to deduced Bravais-lattice type and optimized pattern center and detector distance). We introduce this important tolerance factor for distinguishing between true and false Bravais-lattice types (obtained after 3D reconstruction and reduction treatment [3, 12, 25]), among which the true one will show a reasonable small zone-axis discrepancy (after optimization of the pattern center and detector distance). A demonstration of how different tolerance factors affect the final determined Bravais-lattice types is presented below.

Fig. 4 shows a series of determined patterns of the same semiconductor material  $AAsSe_2$  ( $A = Li, Na$ ), each of which exhibits different zone-axis discrepancies. The accelerating voltage for simulating this pattern is 20 kV. The green lines mark the manually defined traces of unknown diffracting planes. Red circles are the intersections and represent unknown zone axes. The blue lines and their intersections indicate the calculated locations of the traces and zone axes according to the determination results, respectively. If we set a relatively large tolerance factor (80 pixels), the result shown in Fig.3a is a primitive cubic unit cell, with the maximum discrepancy between the manually defined (red circles) and the calculated (blue-line intersections) zone axes, 46.57 pixels. If exclude the result of the primitive cubic, the newly determined Bravais unit cell becomes primitive tetragonal (Fig. 4b), with the maximum zone-axis discrepancy of 46.67 pixels. If exclude the previous results, other different unit cells

may appear. For instance, the resultant Bravais unit cell of Fig. 4c is rhombohedral with the maximum zone-axis discrepancy of 19.68 pixels; that of Fig. 4d is base-centered orthorhombic with 40.58 pixels, and Fig. 4e is base-centered monoclinic with 19.79 pixels. The zone-axis discrepancies in Figs. 4a-3e are not due to our proposed band detection method as the same set of manually defined traces and zone axes are used. They originate from the tolerance of the maximum zone-axis discrepancy: Larger values for this tolerance lead to possible unit cells of higher symmetry, which can be incorrect. For the pattern shown in Fig. 4, if we set the tolerance to be 5 pixels, the determination result is a triclinic unit cell and the theoretically derived traces and zone axes coincide with the manually defined ones (Fig. 4f). The maximum zone-axis discrepancy in Fig. 4f is  $< 0.005$  pixel, rendering a well-determined pattern. Its detailed lattice constants are given in Table 1. With respect to the average determination errors, for  $a$ ,  $b$ ,  $c$ , it is  $(0.25 \pm 0.03)\%$ ; for  $\alpha$ ,  $\beta$ ,  $\gamma$ , it is  $0.08^\circ \pm 0.06^\circ$ ; for axial ratios ( $a/b$ ,  $b/c$ ,  $c/a$ ), it is  $(0.05 \pm 0.02)\%$ ; and for crystal orientation (Euler angles)  $Z$ ,  $X$ ,  $Z$ , it is  $0.05^\circ \pm 0.02^\circ$ . In the following, the default value for the tolerance of zone-axis discrepancy is set to be 5 pixels (about 0.5% of pattern width), since we reckon the accuracy of locating zone axes by eye is less than 5 pixels (in the present EBSD patterns).

The second issue is related to definition of the narrowest band widths, which play a key role in correctly determining the Bravais-lattice types. In particular for a given crystal, its unique reciprocal primitive cell with the smallest volume must be reconstructed. This essentially demands the three shortest reciprocal lattice vectors,

which then require the band detection process must define the three narrowest widths for all visible bands. Unfortunately, defining the narrowest band widths is not a simple work to complete, because Kikuchi bands may have higher interference orders. Fig. 5 shows a simulated pattern of  $\text{CuVO}_3$ . In this figure the lines and circles represent manually defined traces and zone axes, respectively. The two white arrowheads mark a high-order interference of a Kikuchi band, whereas the two black arrowheads mark its first-order interference. If one defines the width of that band as the width of its high-order interference, the determined Bravais lattice is triclinic and the volume of the reconstructed three-dimensional reciprocal primitive cell is  $20.20 \text{ nm}^{-3}$ . If we use the first-order interference of that band to define its width, the final determination result is still a triclinic unit cell (Table 1) but the volume of the reconstructed three-dimensional reciprocal primitive cell becomes  $10.10 \text{ nm}^{-3}$  ( $= \frac{1}{2} \times 20.20 \text{ nm}^{-3}$ ). The improperness of only one band definition can lead to distinct determination results. Ideally, the simplest case is that the edges of a band  $(hkl)_i$  are not only clearly definable but also represent its first-order interference, then defining the narrowest width of this band is easy. But in fact,  $(hkl)_i$  with higher interference orders may have their most important first-order interferences either obviously blurred or not detectable at all. Whether the narrowest visible band width may or may not belong to the first-order interference is difficult to judge and our solution is simply a series of educated guesses.

For example, an  $(hkl)$  exhibits two interferences, with orders of 1 and 2, then the band width of the 1<sup>st</sup> order interference approximately equals to 1/2 of the 2<sup>nd</sup> order interference ( $H_1 = H_2/2$ ); similarly, if with orders of 3, 4 and  $n$ , then

$H_1 = H_3/3 = H_4/4 = H_n/n$ , where  $H_n$  represents the length of the reciprocal vector corresponding to the  $n^{\text{th}}$  order interference. Higher-order interferences of the same  $(hkl)$  always show wider bands, and their dimensions and edges are often clearly better definable than the narrower lower-order interferences, especially the first-order one. After carefully measuring the width of the Kikuchi band in Fig. 5, the two white arrowheads actually mark the 2<sup>nd</sup> order interference of the band, while its narrowest 1<sup>st</sup> order interference is marked by the two black arrowheads. Using the 1<sup>st</sup> order interference, the determination result given in Table 1 is more reasonable than that using the 2<sup>nd</sup> order interference (not shown in this table).

The third issue concerns locating the trace of a diffracting lattice plane from identified zone axes. Manually locating the traces of the first four diffracting planes can have relatively large errors, but these errors can be significantly decreased after the trace-position refinement steps (described in Section 3). On the other hand, the subsequent definition of all other diffracting planes' traces needs a clear identification of proper zone axes. Specifically, the subsequent trace definition is actually a semi-automatic operation which requires manually linking the intersections (zone axes) already formed by previously defined traces. If a trace (representing a diffracting lattice plane  $(hkl)$ ) were wrongly linked to an intersection  $[uvw]$  where its tautozonal planes should not include the plane  $(hkl)$ , the final determination result must be wrong (or no result at all). This problem is caused by the choice of intersections which are sometimes so crowded in local regions that the manual definition can hardly differentiate them.

Fig. 6 displays a simulated EBSD pattern of  $\text{Cu}_3\text{Fe}_4(\text{PO}_4)_6$ . The green lines represent the virtual traces of diffracting but unknown lattice planes  $(hkl)_i$ . Red circles are the intersections and represent unknown zone axes  $[uvw]_m$ . A blue line marks a possible trace of a diffracting plane  $(hkl)$  whose real trace is ambiguous. Because of the locally crowded intersections as shown in a white square (and its magnification shown in the lower-right corner), it is apparent that there are several intersections  $[uvw]_m$  which locate so close to the trace of the Kikuchi band (marked by a blue line) that it is nearly impossible to identify the right zone axes which can properly describe the trace of  $(hkl)$ . If the trace of  $(hkl)$  (marked by the blue line) were defined with wrong zone axes, no correct result will be obtained. The above problem can exist for all the plane traces defined from crowded zone axes; therefore we cannot ascertain whether the final determination result is correct.

To solve this problem, our solution is simply to avert the ambiguous bands first: When linking two intersections, one or both of which are too crowded in local regions to be differentiated from their neighbor intersections, this specific trace should be skipped first, leaving the corresponding Kikuchi band undefined. This is to make sure that all the defined traces are reliable and correct. Then we perform the determination based on the already defined bands. Once a determination result is obtained, the still undefined trace and its band edges can be theoretically calculated by designating two possible intersections on the trace. The calculated and the undefined band edges need to coincide. Hence, by comparing the calculated traces and hyperbolic lines with the actual Kikuchi bands in the pattern, the undefined bands as well as their ambiguous

zone axes (intersections) can be clarified at last. It should be pointed out that using a high screen resolution, i.e., magnifying the EBSD pattern shown in the screen, is beneficial to differentiating the crowded intersections and mitigating this problem.

The last issue is that the reliability and accuracy of the unit-cell determination can be affected by the number of Kikuchi bands that have been detected. Fig. 7a shows a simulated pattern superimposed with only 20 Kikuchi bands detected. The determination result is none. The reason (similar to the second issue above) is that the number of Kikuchi bands that have been detected is so limited that the three narrowest band widths for reconstructing the smallest three-dimensional reciprocal primitive cell of the unknown phase cannot be found in the detected 20 Kikuchi bands. As a result, no appropriate Bravais unit cells can be used to index all the 20 already detected bands. To gain a high probability of finding the smallest primitive cell of a given crystal, the detected Kikuchi bands should be as many as possible, in order to increase the reliability of the determination results.

Fig. 7b displays the same pattern with 40 Kikuchi bands detected. The determination result is a triclinic unit cell ( $a = 5.449 \text{ \AA}$ ,  $b = 6.559 \text{ \AA}$ ,  $c = 7.744 \text{ \AA}$ ,  $\alpha = 96.23^\circ$ ,  $\beta = 90.05^\circ$ ,  $\gamma = 101.26^\circ$ ,  $Z = -9.89^\circ$ ,  $X = 20.07^\circ$ ,  $Z = -30.23^\circ$ ). With respect to the average determination errors, for  $a$ ,  $b$ ,  $c$ , it is  $(1.97 \pm 0.19)\%$ ; for  $\alpha$ ,  $\beta$ ,  $\gamma$ , it is  $0.18^\circ \pm 0.11^\circ$ ; for axial ratios ( $a/b$ ,  $b/c$ ,  $c/a$ ), it is  $(0.31 \pm 0.12)\%$ ; and for crystal orientation (Euler angles)  $Z$ ,  $X$ ,  $Z$ , it is  $0.14^\circ \pm 0.07^\circ$ , which looks reasonable but still noticeably different from both the CIF data ( $a = 5.5703 \text{ \AA}$ ,  $b = 6.6741 \text{ \AA}$ ,  $c = 7.9032 \text{ \AA}$ ,  $\alpha = 96.2^\circ$ ,  $\beta = 90.3^\circ$ ,  $\gamma = 101^\circ$ ) of  $\text{FeVMoO}_7$  and the preset Euler angles ( $-10^\circ$ ,  $20^\circ$ ,



$-30^\circ$ ) for pattern simulation (cf. Table 1). Fig. 7c shows a determined pattern with 80 detected bands forming 889 zone axes. The corresponding result becomes more accurate and confirms that the simulated pattern originates from a triclinic phase (Table 1).

The results summarized in Table 1 can demonstrate the accuracy of determining triclinic unit cells using the proposed method described in Section 3. Compared with corresponding materials' reference lattice parameters in their CIF files and the preset crystal orientations used for simulating the EBSD patterns, the determination results for high-quality patterns are surprisingly good. The average relative error of the unit-cell axes ( $a, b, c$ ) is  $(0.15 \pm 0.09)\%$  and that of the axial ratios ( $a/b, b/c, c/a$ ) is  $(0.12 \pm 0.12)\%$ . The average absolute error of the inter-axial angles ( $\alpha, \beta, \gamma$ ) is  $0.10^\circ \pm 0.07^\circ$  and that of the Euler angles ( $Z, X, Z$ ) is  $0.07^\circ \pm 0.05^\circ$ . Generally speaking, for lattice parameter determination, quantitative determination requires the relative error better than 3%, whereas for accurate determination the number is 0.3%. Therefore, it is evident from Table 1 that the accuracy of determining unknown triclinic unit cells via our proposed method is high, if the pattern quality is high as well.

As a summary of the aforementioned sources of errors when applying the proposed method to determine the Bravais unit cell using an EBSD pattern, we make four recommendations:

- a) The tolerance values for the maximum discrepancy between manually defined and theoretically derived zone axes should be appropriate, which depends on the experimental conditions (e.g., pattern resolution and detector distance) as well as

the accuracy of the band detection. For an ideal crystal without lattice distortion and defects (which will cause zone-axis deviation [33]), five pixels (about  $0.2^\circ$  or 0.5% of pattern width) is a recommended value for a reliable unit-cell determination. While too large tolerance values for the zone-axis discrepancy are obviously not recommended, too small tolerance values are not favorable either, because most crystals are not perfect and their zone axes in EBSD patterns will deviate from their theoretical positions. In the case of imperfect crystals, a slightly larger tolerance value (than the recommended  $0.2^\circ$ ) is also acceptable for a reasonable unit-cell determination.

- b) The three narrowest widths of all visible Kikuchi bands must be defined (in order to reconstruct the smallest reciprocal primitive cell), otherwise incorrect results corresponding to non-primitive cells in the reciprocal space may appear.
- c) The Kikuchi bands likely to be wrongly defined by two zone axes because of the zone-axis over-crowdedness should be skipped first. These bands can be added afterwards according to the determination result.
- d) The detected Kikuchi bands should be as many as possible, so that the determination results show a high degree of confidence.

These four recommendations, even though summarized from determining simulated EBSD patterns, are equally applicable to experimentally collected patterns. For instance, due to the poorer quality of experimental patterns, the number of completely visible bands is small; most band edges appear highly blurred; many bands (or rather hyperbola segments) are only distinguishable in local regions; besides, pattern

center and detector distance cannot be accurately ascertained or sometimes even completely unknown. In these cases, the advantages of our proposed methodology (Steps i–x in Section 3) will become more obvious. Already validated by our thousands of tests, a band-width measurement error less than 20% is sufficient to enable a correct determination of the Bravais-lattice type because as many as possible Kikuchi bands that are visible in an EBSD pattern are involved in the least-square analyses. The pattern center and detector distance can be initially estimated and finally optimized according to the determined Bravais-lattice type and the indices of Kikuchi bands and zone axes. Given a real pattern of low resolution and poor diffraction contrast, only clearly visible bands need to be defined, or even only one relatively clear band is essentially needed. Other ambiguous or blurred bands will be correctly defined after a determination result is obtained by matching the calculated traces and hyperbolae with real Kikuchi bands in the pattern. This post-result band detection also has another advantage: The determination result can be self-verified as it must be consistent with all the visible (even highly blurred) bands in the experimental pattern. It should be emphasized that an EBSD pattern of poor diffraction contrast will make accurate location of the zone axes hard, which in turn decreases the accuracy of axial ratios and inter-axial angles and crystal orientation. Therefore, acquiring high-quality EBSD patterns is always vital in accurate characterizations, especially for determination of unknown Bravais unit cells.

Fig. 8 shows an experimental EBSD pattern collected from the mineral anorthite ( $\text{CaAl}_2\text{Si}_2\text{O}_8$ ) [34]. The green lines denote the traces of diffracting lattice planes. The

four Kikuchi poles indicated by red circles are used to refine the positions of all detected traces, i.e., perform the Step iv in the methodology described in Section 3. As for the pattern center and detector distance of this experimental pattern, neither experimental parameters were given in the reference [34] and need to be found out. To this end, and also for determining the absolute dimensions of lattice constants, we vary the two parameters according to the degree of match between the experimental pattern and the calculated patterns (based on determined Bravais unit cells), i.e., finding the most accurate description of all visible bands with the lowest discrepancy. The estimated pattern center is marked by a yellow cross in Fig. 8, and the estimated detector distance is 0.765. The red hyperbolas are calculated band edges based on a determined unit cell ( $a = 8.252 \text{ \AA}$ ,  $b = 13.069 \text{ \AA}$ ,  $c = 7.240 \text{ \AA}$ ,  $\alpha = 92.38^\circ$ ,  $\beta = 115.66^\circ$ ,  $\gamma = 91.43^\circ$ ). It must be pointed out that this result is not a direct output of our proposed method, but obtained through a crystallographic transformation process, which is detailed in the following.

After determining the experimental pattern shown in Fig. 8, the direct output of a three-dimensional reconstruction procedure (accomplished by *EBSDL* [15]), combined with our proposed band-detection method, is:  $a_0 = 7.240 \text{ \AA}$ ,  $b_0 = 7.641 \text{ \AA}$ ,  $c_0 = 7.815 \text{ \AA}$ ,  $\alpha_0 = 115.47^\circ$ ,  $\beta_0 = 101.18^\circ$ ,  $\gamma_0 = 105.63^\circ$ . This set of unit-cell constants for anorthite appears quite distinct from those reported by literatures [35, 36], as summarized in Table S1 (in the supplementary material). However, it should be emphasized that with our proposed method only a primitive unit cell will be reconstructed for the triclinic Bravais lattice. According to the determined unit-cell constants, the volume of the unit cell in real space can be calculated to be  $351.22 \text{ \AA}^3$ , almost half that of the reported ones

shown in Table S1 (which are in the range from 663.23 Å<sup>3</sup> to 671.19 Å<sup>3</sup>). Furthermore, Table S2 gives the atomic coordinates in the unit cell of anorthite reported in reference [36]; this crystal structure will show (100) and (010) extinction in the single-crystal diffraction, which should not occur for the primitive triclinic Bravais unit cell. This implies that the difference in the unit-cell constants might be caused by the choice of different basis vectors of a triclinic unit cell. Fig. S1 shows a projection of the anorthite unit cell along its reported *c*-axis. It can be found that the reported unit cell (yellow background) is not a primitive cell (which actually is ‘base-centered triclinic’ and does not belongs to the 14 Bravais-lattice types), whereas the basis vectors of a real primitive unit cell for the triclinic lattice of anorthite can be defined as

$$\begin{aligned}\vec{a}_0 &= -\vec{c} & \vec{a} &= \vec{b}_0 + \vec{c}_0 \\ \vec{b}_0 &= \vec{a} / 2 + \vec{b} / 2 & \text{or} & \vec{b} = \vec{b}_0 - \vec{c}_0 \\ \vec{c}_0 &= \vec{a} / 2 - \vec{b} / 2 & \vec{c} &= -\vec{a}_0\end{aligned}$$

where  $\vec{a}_0$ ,  $\vec{b}_0$ ,  $\vec{c}_0$  are the basis vectors of a primitive triclinic unit cell (as indicated by the green background in Fig. S1), and  $\vec{a}$ ,  $\vec{b}$ ,  $\vec{c}$  are the basis vectors of the reported unit cell (yellow background). Based on the above relationship between the two sets of basis vectors, the atomic coordinates in a primitive triclinic unit cell can be calculated, as listed in Table S3. It should be emphasized that within the reported unit cell (containing 56 atoms, cf. Table S2), only half of all atoms (namely, 28) can form the primitive triclinic unit cell (cf. Table S3); what is important is that the other half atoms after coordinate transformation according to above basis-vector relation can exactly coincide with the atoms (including their positions and types) in the primitive triclinic unit cell. Therefore, Tables S1–S3 confirm that the previously reported triclinic

unit cell for anorthite is indeed a non-primitive unit cell. The direct determination result mentioned above is a primitive Bravais unit cell ( $\vec{a}_0$ ,  $\vec{b}_0$ ,  $\vec{c}_0$ ,  $\alpha_0$ ,  $\beta_0$ ,  $\gamma_0$ , as indicated in Fig. S1), with the transformed result (to the reported non-primitive unit cell) shown in Table 1, which demonstrates that the triclinic Bravais unit cell can be successfully determined by three-dimensional reconstruction combined with our proposed band-detection method using a single EBSD pattern.

With respect to the determination accuracy, since the exact lattice constants of anorthite for the experimental pattern (Fig. 8) are unavailable (which depends on material composition, internal stress, etc.), we take the average published values (of Table S1) as a source of reference lattice constants [35, 36]. Moreover, both the pattern center and the detector distance are not exactly known, which have a significant impact on the inter-axial ratios and angles (their accuracy can be significantly improved if both were known). The uncertainty of the incoming/diffracting beam energy makes

measurement of the band widths less precise, which may also lead to increased determination errors [37].

Consequently, the specific values of the calculated errors (Table 1) can only serve as a rough estimate for determining the experimental pattern. Additionally, we also determine another experimental pattern (Fig. 9) collected from the mineral andesine  $[(\text{Ca},\text{Na})(\text{Al},\text{Si})_4\text{O}_8]$  [38]. This case is very similar to anorthite, i.e., the reported triclinic unit cells in literatures (as summarized in Table S4, [35, 39-43]) are actually not a primitive triclinic Bravais unit cell. The direct determination result by our method is:  $a_0 = 7.143 \text{ \AA}$ ,  $b_0 = 7.534 \text{ \AA}$ ,  $c_0 = 7.577 \text{ \AA}$ ,  $\alpha_0 = 114.68^\circ$ ,  $\beta_0 = 101.94^\circ$ ,  $\gamma_0 = 105.08^\circ$ , with a unit-cell volume  $333.82 \text{ \AA}^3$ . The transformed result and

corresponding accuracy are also given in Table 1, and the related crystallographic transformation process, which includes Fig. S2 and Tables S5–S6 showing the atomic coordinates in the two different unit cells, is demonstrated in the supplementary material. Overall, the determined unit-cell constants for the experimental patterns (Figs. 8–9) are generally in good agreement with the published values, which further confirms the high reliability of our proposed method.

Finally, limitations and future development of our method are stated. It was initially designed only for determining all the 14 types of Bravais unit cells (of which we make a classification according to determined unit-cell constants, instead of crystal symmetry), with a design objective: Even in the case of obvious band-width measurement error (up to 20%) and completely unknown projection center, a single EBSD pattern from an unknown crystal (without any possible material candidates) enables an accurate determination of its lattice constants and crystal orientation. However, neither the 32 crystallographic point groups nor a whole crystal structure (including atomic types and positions and space groups) can be determined by our method. This is because it is purely based on the definition of diffracting-plane traces and band widths as well as the geometric 3D reconstruction, without considering crystal symmetry. Determination of the crystallographic symmetries by EBSD requires a full inspection of the diffraction intensity features of zone axes [2, 3, 44, 45]. Strictly speaking, our method cannot correctly determine a triclinic crystal with lattice constants ( $a = b = c$ ,  $\alpha = \beta = \gamma = 90^\circ$ ), in which case an incorrect cubic crystal would be the result. Up to now, the 14 types of Bravais unit cells are differentiated only by the six lattice

constants determined. Our future work is to take into account the symmetric features of zone axes after correcting the gnomonic distortion of EBSD patterns, in order to make the EBSD technique a powerful experimental tool for high-accuracy and high-reliability unit-cell determination.

## 5. Conclusions

A new method on the basis of recently developed three-dimensional reconstruction using single EBSD pattern has been proposed for determining the unknown phases of low symmetry. It is purely based on diffraction geometry: neither prior knowledge about the sample's chemical composition nor a database is requisite. It enables a semi-automated decrease in the random errors involved during the band detection process, and thus could considerably improve the EBSD technique for accurate lattice-constant determination of unknown phases. Testing of the method on several triclinic crystals proves it to be practical, with a reasonably high accuracy. By using simulated EBSD patterns, the relative error of the unit-cell constants ( $a$ ,  $b$ ,  $c$ ) is less than 0.3%, and that of the axial ratios ( $a/b$ ,  $b/c$ ,  $c/a$ ) is less than 0.5%. The absolute errors of the inter-axial angles ( $\alpha$ ,  $\beta$ ,  $\gamma$ ) and the Euler angles ( $Z$ ,  $X$ ,  $Z$ ) are about  $0.1^\circ$ .

The requisites for applying the proposed method to experimental patterns are flexible. The analyzed materials may belong to any crystal symmetry with random orientations. High-quality EBSD patterns are beneficial to the final determination accuracy, whereas a single low-quality (relatively vague) pattern does not exclude the possibility of acquiring a reliable determination result, because only one relatively clear band needs to be well defined (rather than a completely high-quality pattern), which



makes the advantage of our proposed method more obvious when treating usually blurred experimental patterns. Other instrumental and experimental requirements follow those of conventional EBSD in SEM. Our method could be easily incorporated into an SEM and may become an important development in the evolution of the microanalysis techniques.

### **Acknowledgements**

This work is supported by the Natural Science Foundation of China under grant No. 51071125, Major Project of Natural Science Foundation of Jiangxi Province under grant No. 20161ACB20010, the Hong Kong Research Grants Council through the Early Career Scheme (Project No. 25301617) and the Hong Kong Polytechnic University grant (Project No. 1-ZE6G). The authors would like to give special thanks to Bruker Nano GmbH for providing the software DynamicS, which makes feasible the verification of the software *EBSDL*.

### **References**

- [1] H.P. Klug, L.E. Alexander, X-ray diffraction procedures for polycrystalline and amorphous materials, 2nd ed., John Wiley & Sons, New York, 1974.
- [2] D.J. Dingley, K.Z. Baba-Kishi, V. Randle, Atlas of backscattering Kikuchi diffraction patterns, Bristol; Philadelphia, Pa. : Institute of Physics Pub., 1995.
- [3] D.J. Dingley, S.I. Wright, Determination of crystal phase from an electron backscatter diffraction pattern, J. Appl. Cryst., 42 (2009) 234-241.
- [4] V.K. Pecharsky, P.Y. Zavalij, Fundamentals of powder diffraction and structural characterization of materials, 2nd ed., Springer, Boston, US, 2009.

- [5] T.B. Britton, C. Maurice, R. Fortunier, J.H. Driver, A.P. Day, G. Meaden, D.J. Dingley, K. Mingard, A.J. Wilkinson, Factors affecting the accuracy of high resolution electron backscatter diffraction when using simulated patterns, *Ultramicroscopy*, 110 (2010) 1443-1453.
- [6] M.E. Straumanis, E.Z. Aka, Lattice Parameters, Coefficients of Thermal Expansion, and Atomic Weights of Purest Silicon and Germanium, *Journal of Applied Physics*, 23 (1952) 330-334.
- [7] J. Bačkovský, On the most accurate measurements of the wavelengths of X-ray spectral lines, *Czechoslovakij fiziceskij zurnal B*, 15 (1965) 752-759.
- [8] B.D. Cullity, *Elements of X-ray diffraction*, Addison-Wesley Publishing Company, Inc., USA, 1956.
- [9] W. Parrish, Results of the IUCr precision lattice-parameter project, *Acta Crystallographica*, 13 (1960) 838-850.
- [10] G. Changlin, X-ray diffraction methods for accurate measuring the lattice constants of polycrystalline materials with low-symmetry system, *J. Inorg. Mater.*, 11 (1996) 597-605.
- [11] J.R. Michael, J.A. Eades, Use of reciprocal lattice layer spacing in electron backscatter diffraction pattern analysis, *Ultramicroscopy*, 81 (2000) 67-81.
- [12] L. Li, M. Han, Determining the Bravais lattice using a single electron backscatter diffraction pattern, *J. Appl. Cryst.*, 48 (2015) 107-115.
- [13] L. Li, M. Han, A novel way for determining Bravais lattice using a single electron backscatter diffraction pattern, *Microsc. Microanal.*, 21 (2015) 2375-2376.

- [14] L. Li, M. Han, The determination of lattice parameters using single EBSD patterns, *Microsc. Microanal.*, 22 (2016) 634-635.
- [15] L. Li, S. Ouyang, Y. Yang, M. Han, EBSDL: a computer program for determining an unknown Bravais lattice using a single electron backscatter diffraction pattern, *J. Appl. Cryst.*, 47 (2014) 1466-1468.
- [16] M. Han, L. Li, G. Xiong, H. Luo, Y. Wan, Method for determining 3D primitive reciprocal basis of unknown crystal based on single EBSD pattern, in: U.S.P.a.T. Office (Ed.), East China Jiaotong Univesity, U.S.A., 2017.
- [17] M. Han, C. Chen, G. Zhao, L. Li, G. Nolze, B. Yu, X. Huang, Y. Zhu, Blind lattice parameter determination of cubic and tetragonal phases with high accuracy using a single EBSD pattern, *Acta Crystallogr. A*, (2018) (Accepted).
- [18] L. Reimer, Scanning electron microscopy physics of image formation and microanalysis, Second ed., Springer, New York, 1998.
- [19] J. Alkorta, Limits of simulation based high resolution EBSD, *Ultramicroscopy*, 131 (2013) 33-38.
- [20] L. Li, M. Han, G. Xiong, H. Luo, Y. Wan, Method for determining geometric relationships of crystal reciprocal vectors on two-dimensional planes obtained from single EBSD pattern, in: U.S.P.a.T. Office (Ed.), East China Jiaotong Univesity, U.S.A., 2016.
- [21] C.S. Weiss, Ueber mehrere neubeobachtete Krystallflächen des Feldspathes, und die Theorie seines Krystallsystems im Allgemeinen, *Abh. K. Akad. Wiss. Berlin.*, (1820–1821) 145-184.

- [22] A. Authier, *Early Days of X-ray Crystallography*, Oxford University Press, Oxford, 2013.
- [23] N.C.K. Lassen, D.J. Jensen, K. Conradsen, Image processing procedures for analysis of electron back scattering patterns, *Scanning Microsc.*, 6 (1992) 115-121.
- [24] G. Nolze, A. Winkelmann, Crystallometric and projective properties of Kikuchi diffraction patterns, *J. Appl. Cryst.*, 50 (2017) 102-119.
- [25] J.R. Michael, Phase Identification Using Electron Backscatter Diffraction in the Scanning Electron Microscope, in: A.J. Schwartz, M. Kumar, B.L. Adams (Eds.) *Electron Backscatter Diffraction in Materials Science*, Springer US, Boston, MA, 2000, pp. 75-89.
- [26] J.R. Rea, P.W. Bless, E. Kostiner, The crystal structure of  $\text{CuVO}_3$ , a distorted ilmenite-type derivative, *J. Solid State Chem.*, 5 (1972) 446-451.
- [27] A. Le Bail, L. Permer, Y. Laligant, Structure of  $\text{FeVMoO}_7$ , *Eur. J. Solid State Inorg. Chem.*, 32 (1995) 883-892.
- [28] T.K. Bera, J.I. Jang, J.-H. Song, C.D. Malliakas, A.J. Freeman, J.B. Ketterson, M.G. Kanatzidis, Soluble semiconductors  $\text{AAsSe}_2$  ( $a = \text{Li, Na}$ ) with a direct-band-gap and strong second harmonic generation: a combined experimental and theoretical study, *J. Am. Chem. Soc.*, 132 (2010) 3484-3495.
- [29] Anonym,  $\text{Cu}_3\text{Fe}_4(\text{PO}_4)_6$ , in: *Crystallography Open Database (COD)*, COD ID: 1000023, 2016.
- [30] A. Winkelmann, C. Trager-Cowan, F. Sweeney, A.P. Day, P. Parbrook, Many-beam dynamical simulation of electron backscatter diffraction patterns,

Ultramicroscopy, 107 (2007) 414-421.

[31] H.J. Bunge, Texture analysis in materials science : mathematical methods, English ed., Butterworths, Boston, 1982.

[32] T.B. Britton, J. Jiang, Y. Guo, A. Vilalta-Clemente, D. Wallis, L.N. Hansen, A. Winkelmann, A.J. Wilkinson, Tutorial: Crystal orientations and EBSD — Or which way is up?, Materials Characterization, 117 (2016) 113-126.

[33] A.J. Schwartz, M. Kumar, B.L. Adams, D.P. Field, Electron backscatter diffraction in materials science, 2nd ed., Springer Science Business Media, New York, NY, 2009.

[34] C. Ma, A.N. Krot, M. Bizzarro, Discovery of dmisteinbergite (hexagonal  $\text{CaAl}_2\text{Si}_2\text{O}_8$ ) in the Allende meteorite: A new member of refractory silicates formed in the solar nebula, Am. Mineral. , 98 (2013) 1368-1371.

[35] H.R. Wenk, W. Joswig, T. Tagai, M. Korekawa, B.K. Smith, The average structure of An 62-66 labradorite, Am. Mineral., 65 (1980) 81-95.

[36] E. Wadoski-Romeijn, T. Armbruster, Topotactic transformation and dehydration of the zeolite gismondine to a novel Ca feldspar structure, Am. Mineral., 98 (2013) 1988-1997.

[37] F. Ram, M. De Graef, Energy dependence of the spatial distribution of inelastically scattered electrons in backscatter electron diffraction, Physical Review B, 97 (2018) 134104.

[38] Y. Xie, H.-R. Wenk, S. Matthies, Plagioclase preferred orientation by TOF neutron diffraction and SEM-EBSD, Tectonophysics, 370 (2003) 269-286.

- [39] M.W. Phillips, A.A. Colville, P.H. Ribbe, The crystal structures of two oligoclases : A comparison with low and high albite, *Zeitschrift für Kristallographie - Crystalline Materials*, 133 (1971) 43.
- [40] K. Toman, A.I. Frueh, On the centrosymmetry of intermediate plagioclases, *Zeitschrift für Kristallographie - Crystalline Materials*, 138 (1973) 337-342.
- [41] W. Horst, T. Tagai, M. Korekawa, H. Jagodzinski, Modulated structure of a plagioclase An<sub>52</sub>: Theory and structure determination, *Zeitschrift für Kristallographie - Crystalline Materials*, 157 (1981) 233-250.
- [42] J.D. FitzGerald, J.B. Parise, I.D.R. MacKinnon, Average structure of an An<sub>48</sub> plagioclase from the Hogarth Ranges, *Am. Mineral.*, 71 (1986) 1399-1408.
- [43] A.F. Gualtieri, Accuracy of XRPD QPA using the combined Rietveld–RIR method, *J. Appl. Cryst.*, 33 (2000) 267-278.
- [44] K.Z. Baba-Kishi, Review Electron backscatter Kikuchi diffraction in the scanning electron microscope for crystallographic analysis, *Journal of Materials Science*, 37 (2002) 1715-1746.
- [45] V. Randle, Applications of electron backscatter diffraction to materials science: status in 2009, *Journal of Materials Science*, 44 (2009) 4211-4218.

### Captions for Table and Figures

**Table 1** Comparison between published (or theoretical) and determined values of six different triclinic materials' lattice constants and/or crystal orientations. The unit of lattice constants  $a, b, c$  is Å; the inter-axial angles  $\alpha, \beta, \gamma$  and the Euler angles  $Z, X, Z$  (arbitrarily set for different materials) are in degree ( $^{\circ}$ ); the error (taking the published values as references) for  $a, b, c, a/b, b/c, c/a$  is in percent (%), and the error for all the angles is in degree ( $^{\circ}$ ).

**Fig. 1** Geometric crystallography of the EBSD: (a) Three-dimensional configuration of the gnomonic projection; (b) Discrepancy between the trace (green) of a diffracting lattice plane ( $hkl$ ) and the center line (red) of a hyperbola-shaped Kikuchi band. The plane ( $hkl$ ) bisects the angle  $2\theta_i$ .  $w_i$  is the band width. O and O' are the pattern center and the source, respectively.

**Fig. 2** Determination of real band edges: a) An experimental EBSD pattern with blurred Kikuchi bands; b) Corrected reciprocal vectors on a reciprocal plane after geometric correction and a two-dimensional fitting grid (green dashed lines) for determining the lengths of reciprocal vectors.

**Fig. 3** The band detection process: (a) pole-dispersion problem, (b) effects of predefining the positions of four non-tautozonal bands, (c) mitigated deviations of the traces and band edges. The green lines are manually defined traces, and red circles are their intersections. The pink hyperbola

segments are derived positions of the band edges. A blue square is magnified in the lower-right corner. The pattern center is marked by a red cross.

**Fig. 4** A determined pattern of a semiconductor material  $AAsSe_2$  ( $A = Li, Na$ ), showing different discrepancies between manually defined and theoretically derived locations of the intersection points (zone axes). (a) The resultant unit cells are (a) primitive cubic with the maximum zone-axis discrepancy 46.57 pixels, (b) primitive tetragonal with the maximum zone-axis discrepancy of 46.67 pixels, (c) rhombohedral (19.68 pixels) (d) base-centered orthorhombic (40.58 pixels), (e) base-centered monoclinic (19.79 pixels), and (f) triclinic ( $< 0.005$  pixel).

**Fig. 5** A simulated pattern of  $CuVO_3$ , showing a Kikuchi band's two orders of interferences.

**Fig. 6** A simulated pattern of  $Cu_3Fe_4(PO_4)_6$ . The intersections are so crowded in local regions that the naked eyes can hardly differentiate between them.

**Fig. 7** A simulated pattern of  $FeVMoO_7$  with different numbers of detected Kikuchi bands: (a) 20 bands, (b) 40 bands, (c) 80 bands.

**Fig. 8** A determined experimental pattern of anorthite ( $CaAl_2Si_2O_8$ ). The accelerating voltage is 15 kV. The estimated detector distance is 0.765 and the pattern center marked by a yellow cross.

**Fig. 9** A determined experimental pattern of andesine  $[(Ca,Na)(Al,Si)_4O_8]$ . The accelerating voltage is 10kV. The estimated detector distance is 0.598 and the pattern center marked by a yellow cross.